

Fermi National Accelerator Laboratory

FERMILAB-Conf-94/035-E
DØ Note 1956
DØ

Studies of Jet Production with the DØ Detector

Harry Weerts

*Michigan State University
East Lansing, Michigan 48824*

*Fermi National Accelerator Laboratory
P.O. Box 500, Batavia, Illinois 60510*

January 1994

Presented at the *9th Topical Workshop on Proton-Antiproton Collider Physics*,
Tsukuba, Japan, October 18-22, 1993

Disclaimer

This report was prepared as an account of work sponsored by an agency of the United States Government. Neither the United States Government nor any agency thereof, nor any of their employees, makes any warranty, express or implied, or assumes any legal liability or responsibility for the accuracy, completeness, or usefulness of any information, apparatus, product, or process disclosed, or represents that its use would not infringe privately owned rights. Reference herein to any specific commercial product, process, or service by trade name, trademark, manufacturer, or otherwise, does not necessarily constitute or imply its endorsement, recommendation, or favoring by the United States Government or any agency thereof. The views and opinions of authors expressed herein do not necessarily state or reflect those of the United States Government or any agency thereof.

Studies of jet production with the DØ detector

Harry Weerts

for the DØ collaboration

Department of Physics & Astronomy, Michigan State University

East Lansing, Michigan 48824, USA

During the first collider run at the Tevatron, the DØ experiment has accumulated a large sample of events with jet final states, covering a jet E_T range from about 30 to 400 GeV and pseudorapidities up to $\eta = 3.2$. First results about the transverse energy flow as a function of the jet cone size R are obtained and presented. The study of the two leading E_T jets in events results in a measurement of the dijet angular distribution $1/\sigma d\sigma/d\chi$ as well as the triple differential cross section $d^3\sigma/dE_T d\eta_1 d\eta_2$ over a rapidity region not explored before. The correlation between E_T of two jets and their distance in pseudorapidity is outlined as a test of resummation techniques and compared to a recent theoretical prediction. Finally distributions are presented characterizing the topology of 3 jet events and they are compared to parton shower Monte Carlo's and to an $O(\alpha_s^3)$ prediction at the tree level.

1. Introduction

The DØ experiment at the Fermilab Tevatron $p\bar{p}$ collider has completed its first successful data run in June of 1993. The experiment was commissioned with colliding beams during the spring of 1992 and started taking data officially in August of 1992. A total luminosity of 16.7pb^{-1} was accumulated, which corresponds to about 13×10^6 events written to tape. This paper describes the current, preliminary status of several analyses involving jet final states. It will start with a description of those detector elements most important for the analysis of jets: the calorimeters. For a more detailed description of other detector elements or a more general description of the complete experiment, see refs. [1, 2]. The next few sections describe the DØ calorimeters, outline the triggers used for jet final states, the algorithm used to define jets and the jet energy determination. The results presented include the jet transverse energy profile or jet shape, dijet cross sections and topological cross sections for 3 jet events. Other studies with jet final states like the total inclusive jet cross section, a search for rapidity gaps between jets and a study of color coherence effects are presented in refs. [3, 4].

2. Jet identification and measurement

2.1 DØ calorimetry

The DØ detector was designed with emphasis on identification and measurement of electrons, muons, jets and missing transverse energy (\cancel{E}_T). This requires uniform, hermetic, finely segmented calorimeter coverage over a large region in pseudorapidity ($\eta = -[\ln \tan(\theta/2)]$) and azimuthal angle (ϕ). This is achieved in DØ with a calorimeter system that employs

uranium as absorber material and liquid argon as the charge sensitive medium. It consists of 3 cryostats: the central part covering pseudorapidity $|\eta| < 1.2$ and the forward calorimeters covering $1.2 < |\eta| < 4.0$. The region $|\eta| < 0.6$ is completely contained by the central part whereas the region $1.2 < |\eta| < 4.0$ is completely contained in the forward part. The overlap region, where sampling is reduced due to the cryostat walls and intercryostat space, contains additional detector elements (scintillator and additional argon gaps without absorber) to compensate for this. The coverage in azimuth is uniform for all ϕ , except for small cracks in the central calorimeter between modules. On the scale of a jet such cracks are completely negligible. The calorimeter has been in operation continuously since February 1992. The change in the response (monitored by argon gaps instrumented with α and β sources[1]) has been less than 0.2% over the last year and the purity of the argon used is better than 0.7ppm of oxygen equivalent.

Longitudinally, the calorimeter starts with an all uranium electromagnetic section, subdivided into 4 depth segments of thickness 2, 2, 7 and 10 radiation lengths (X_0) and equivalent to one interaction length(λ). This is followed by a fine hadronic uranium section consisting of 3 depth segments each 1λ long. The last section is a Cu(central) or Fe(forward) coarse section which accounts for 3λ in the central region and up to 5λ in the forward region. Transversely the segmentation in pseudo-rapidity and azimuth is $\Delta\eta \times \Delta\phi = 0.1 \times 0.1$ up to $\eta = 2.5$ where it doubles in size in both dimensions. This results in a total of about 50,000 electronics channels being read out. The fine transverse and longitudinal segmentation results in a nearly projective tower geometry which makes identification of jets very straightforward. The noise characteristics of the calorimeter are excellent. Typical noise depends on the size of the cell and varies from 15 MeV/cell in the electromagnetic sections to 70 MeV/cell in the fine hadronic sections. This noise is completely dominated by fluctuations in the dark current generated by the uranium radioactivity. The least count for a cell is 3-5 MeV/cell depending on the sampling fraction of the cell. Minimum ionizing particles can be easily observed and calorimeter confirmation is required for muon candidates. The energy response of the calorimeters to single electrons and pions has been measured between 2 and 150 GeV in a testbeam [5]. The response was found to be linear down to 10 GeV, within 1% for electrons and within 3% for pions. For lower energies down to 2 GeV non-linearities up to 12% were observed for electrons and up to 15% for pions. The fractional energy resolution for electrons was measured to be $\sigma/E = .003 + 0.15/\sqrt{E}$ and the corresponding results for pions was: $\sigma/E = .04 + 0.50/\sqrt{E}$. The response of electrons relative to pions (e/π) was determined to be less than 1.03 for energies above 50 GeV and slowly increases with decreasing energy to about 1.09 at 10 GeV.

The single particle response measured at the testbeam has been transferred to DØ and it is this response which is being used for the initial jet energy scale in this paper. Corrections to the jet energy which arise from nonlinearities in the single particle response and other instrumental effects are described in sect. 2.4.

2.2 Triggering on jets

The first requirement for any trigger, during the first data taking run, was that the beam beam or luminosity counters [1] fire, indicating an inelastic collision. The timing information from these counters can be used to limit the vertex position of the interaction to be in the center of the detector. This is done for prescaled triggers as to fully exploit the projective

geometry of the detector. At the first level(L1) of the trigger, which does not incur any deadtime, calorimeter information is available in $\Delta\eta \times \Delta\phi = 0.2 \times 0.2$ non-overlapping towers summed over all electromagnetic depths or summed over the electromagnetic and fine hadronic depths. The latter configuration is used to trigger on jets. A jet trigger at this level in general consists of requiring one or more trigger towers, possibly in selected η, ϕ regions, to be above threshold. Because the number of thresholds available for each trigger tower is limited to 4 , a jet trigger either requires one tower above a threshold or more than one tower to be above threshold. On average a trigger tower contains about 1/3 of the total jet energy, but because of the width of the distribution a trigger does not become $> 95\%$ efficient until jet transverse energies (E_T) that are approximately 6 times the L1 threshold. Data available for this paper only used a trigger instrumented for $|\eta| < 3.2$ and the data shown are all with this restriction. Currently the trigger is being extended to $|\eta| = 4$.

Events passing the L1 jet triggers are passed to the level-2 (L2) trigger, which is a software trigger. The L2 system consists of an array of 48 microVAX processors. Each processor contains the same code which is a set of software filters, activated depending on the L1 triggers fired for a particular event. Here only the parts pertinent to jet triggers will be described. At L2 a fixed cone algorithm (see sect.2.3) with a cone size $\Delta R = 0.7$ is used. The trigger towers found above threshold in L1 are used as seed positions for this algorithm. An inclusive type trigger was used, i.e. only one jet in the event was required to be above threshold. To map the complete, rapidly falling E_T spectrum five thresholds were used: 20, 30, 50 , 85 and 115 Gev. The lower thresholds were prescaled and the corresponding luminosity written to tape for each threshold reflects this: 13, 130, 1050, 6950 and 14,800 nb⁻¹. The results described in this paper are all derived from these inclusive triggers. Here inclusive means: the event is accepted if one of the final state jets passes the threshold. For special purposes other more specialized triggers were employed: for example a trigger which requires two jets in the final state with a specified distance in rapidity between the jets or to increase the statistics at moderate jet E_T 's in the forward regions, special forward triggers were employed. These trigger conditions can be applied at L1 and then reinforced at L2. In general the trigger system is very flexible and detailed final topologies can be triggered on .

2.3 Jet algorithm and selection

A jet, unlike a muon, electron or photon, is not a well defined object at the partonic level nor at the particle or the calorimeter level, which are observed in the detectors. The availability of next to leading order QCD predictions has made it necessary to define jets at the parton level, because a jet can consist of more than one parton. The definition most commonly used (and exclusively used in $p\bar{p}$ physics) is the fixed cone algorithm [6]. This algorithm uses a fixed cone in η, ϕ space. All energy within a cone $\Delta R = \sqrt{\Delta\eta^2 + \Delta\phi^2}$ is assigned to the jet . The algorithm starts by using all towers (size: $\Delta\eta \times \Delta\phi = 0.1 \times 0.1$ and summed over all depths), with $E_T > 1\text{GeV}$ as seed towers. For each seed a jet with a $\Delta R = 0.7$ is constructed. For each jet the transverse energy (E_T), and direction (η, ϕ) are determined using Eqs. 1-3. The new position is used as the center of the new cone and the procedure is repeated until the jet direction is stable. The index i in the equations runs over all cells within the jet cone. The default jet cone size is $\Delta R = 0.7$.

$$E_k = \sum_i E_k^i \quad k = x, y, z , \text{ total energy} \quad i = \text{all cells in the cone} \quad (1)$$

$$E_T^i = \sqrt{E_x^i{}^2 + E_y^i{}^2} \quad E_T = \sum_i E_T^i \quad (2)$$

$$\phi = \arctan E_y/E_x \quad \theta = \arccos E_z/\sqrt{E_x^2 + E_y^2 + E_z^2} \quad \eta = -\ln \tan \theta/2 \quad (3)$$

These definitions do not exactly follow the so-called Snowmass Accord [7] where the jet direction is determined by E_T weighted means of η and ϕ . For centrally produced jets the jet direction obtained that way and by using Eqs. 1-3, are nearly identical. However for forward produced jets ($|\eta| > 2.0$), there is a systematic difference and the Snowmass Accord prescription is less accurate.

If the distance in η, ϕ space between two jet axes is smaller than 0.7 the two jets possibly overlap and it is not clear whether it is one or two jets. The criteria used to merge two jets into one is the following: consider two jets with transverse energies E_T^1 and E_T^2 and define E_T^{sh} as the transverse energy shared by both jets. If $E_T^{sh}/\min(E_T^1, E_T^2) > 0.5$ the two jets are considered one and their parameters are redetermined. If this condition is not true then the two jets are kept as separate jets and the energy of a cell in the overlap region is assigned to the jet whose jet axis is the closest to the cell. It should be noted that although the same algorithm is used to define jets at the parton and calorimeter level, the splitting and merging criteria used are different because they have to be based on different observables[13]. Offline jets are reconstructed with the above described jet algorithm and all jets with $E_T > 8$ GeV are retained. For analysis purposes E_T cuts are applied such that they are about 10-15 GeV above the thresholds used in the L2 filters. This assures that overall the trigger efficiency over the whole detector is greater than 95%. At this stage some cuts are applied to remove remaining noise and background:

- to remove noisy cells, require the fractional jet energy in the electromagnetic section (em_{frac}) $0.05 < em_{frac} < 0.95$
- energy in 2nd most energetic cell/ energy in most energetic cell > 0.10
- fractional energy in the coarse hadronic calorimeter part, containing the main ring accelerator, < 0.40
- $E_T/E_T^{leadingjet} < 0.7$. This cut removes essentially high E_T jets due to spurious noise and cosmic rays.

Applying these cuts results in an efficiency for retaining good jets of $(97 \pm 0.3)\%$ at $E_T = 30$ GeV which slowly decreases to $(89 \pm 3)\%$ at $E_T = 410$ GeV. These cuts are applied to all DØ jet analyses to remove calorimeter noise, main ring accelerator background, cosmic ray noise and background from instrumental sources.

2.4 Jet energy scale and resolution

As already mentioned in section 2.1 the energy response to single particles of the calorimeters was determined in a testbeam. The energy scale measured there was transferred to the DØ detectors at the collider and this single particle energy scale was used for triggering and online purposes. A jet is not a single particle, but a large collection of particles and most of them are at low momenta. For example 70% of the energy of a centrally produced 50 GeV jet is made up by particles with individual momentum less than 5 GeV. Because of non

linearities in the response, especially at particle energies below 10 GeV, and variations in the response due to poorly instrumented regions, the measured jet energy has to be corrected to get the true jet energy. Here we define the true jet energy (E^c) as the energy of all particles contained in a cone $\Delta R = 0.7$ around the jet axis. The measured jet energy (E^m) is the energy determined in the calorimeters using the single particle response and again a cone of size $\Delta R = 0.7$. The corresponding transverse jet energies are defined as E_t^m and E_t^c . The current correction technique is based on using collider data only and consists of two steps: 1) get the correct energy scale in the central region ($|\eta| \leq 0.7$) and 2) transfer this corrected energy scale to the forward region ($|\eta| > 0.7$). These steps are outlined in the following.

To obtain the correct energy in the central region the Missing Transverse Energy Projection Fraction (MPF) is used. This method, introduced by CDF [9], is used in a slightly modified fashion in events which have a jet and a photon in the final state. Both objects are required to be in the central region and the photon is defined as an isolated cluster of energy contained in the electromagnetic section of the calorimeter i.e. $< 5\%$ of the energy is deposited in the hadronic section. So although it is called a photon these clusters consist of photons and/or π^0 's and their energy scale is completely determined by the electromagnetic energy response (R_{em}). $R_{em} = 0.956$ and this is obtained by shifting the nominal testbeam response such that the Z mass, reconstructed from $Z \rightarrow e^+e^-$ decays, equals the value measured at LEP. For the selected event configuration the missing transverse energy vector (\vec{E}_T) is calculated by summing the calorimeter information over all η, ϕ and all depths. The quantity MPF is defined by Eq. 4, where \vec{n}_t is the unit vector along the measured transverse jet axis and E_t^m is the measured transverse energy of the jet as defined above.

$$MPF = \frac{\vec{E}_T \cdot \vec{n}_t}{E_t^m} \quad R_{jet} = \frac{1}{(1 + MPF)} \quad (4)$$

So MPF is the component of the \vec{E}_T , relative to E_t^m , projected on the transverse jet direction. Compared to using simple transverse momentum balancing, this method minimizes the sensitivity to other jets being present in the event. In addition it does not automatically correct for energy deposited uniformly outside the jet cone used, because this energy does not contribute to \vec{E}_T . The jet response (R_{jet}) of the calorimeter, relative to the electromagnetic response R_{em} , is given by the second part of Eq. 4. This response is shown in Fig. 1 as a function of E^m . The solid line indicates the fit used for all further discussions and the current, conservative error band is given by the two dotted lines. The MPF method has been verified by a Monte Carlo simulation where the single particle response is modeled based on the nonlinear response measured in the testbeam. The jet response is then calculated based on the MPF method and using the known non linear response. For jet energies above 10 GeV the difference between the real response and the MPF determined response is less than 5% everywhere. Based on this, a rather conservative systematic error of 5% is currently assigned to using the MPF method.

Correcting E^m with the jet response results in the correct energy in the cone in the calorimeter. This is not equal to the true jet energy, E^c , yet because of the following corrections:

- The combination of zero suppression and asymmetric pedestal distributions caused by the uranium noise give rise to a systematic shift in the energy. In addition there

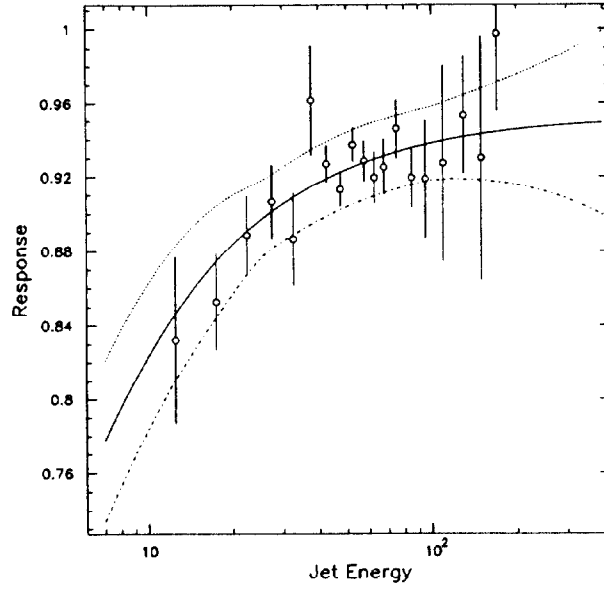


Figure 1: Calorimeter response R_{jet} for jets versus jet energy.

is a contribution from the underlying event. The shift due to zero suppression was determined by taking data without zero suppression and the underlying event was assumed to be equal to the contribution measured in minimum bias events. For the default cone size $\Delta R = 0.7$ these effects contribute an extra 3 GeV transverse energy in the central region, which has to be subtracted.

- Particles which are part of the jet and are contained within the jet cone, deposit their energy in the calorimeter in showers with a finite transverse size. The fraction of the energy deposited outside the cone (“out of cone correction”) is on average 4% and was determined from testbeam showers.

Applying all these corrections and R_{jet} to E^m results in the true jet energy (E^c) in the central region.

In a second step this jet energy scale is transferred to the forward region. This is done by using P_T balance in two jet events which have a central jet and a probe jet, which can be anywhere in rapidity. The reason for using P_T balance instead of the *MPF* method is twofold: 1) the zero suppression and underlying event correction in the forward region are automatically taken into account. 2) In the forward region out of cone corrections are larger (up to 15%) because the jet cone size is fixed in rapidity, while the transverse size of a shower covers more units of rapidity in the forward region than in the central region. Two jet P_T balance takes care of this automatically. The resulting correction factor ($=E_t^c/E_t^m$) is shown in Figure 2 for two different values of pseudorapidity. The fact that the correction does not increase at low E_T is due to the contributions from zero suppression and underlying event which have to be subtracted (see above). The error band shown consists of the systematic error in the *MPF* method, discussed above, and added to it in quadrature a 5% uncertainty in fits and additional corrections.

After the jet energy correction is applied the jet energy resolution is obtained by using a sample of two jet events and constructing the quantity $A = (E_t^1 - E_t^2)/(E_t^1 + E_t^2)$. The fractional transverse jet energy resolution is simply related to the error in the quantity A by

DØ Jet Energy Correction R=.7

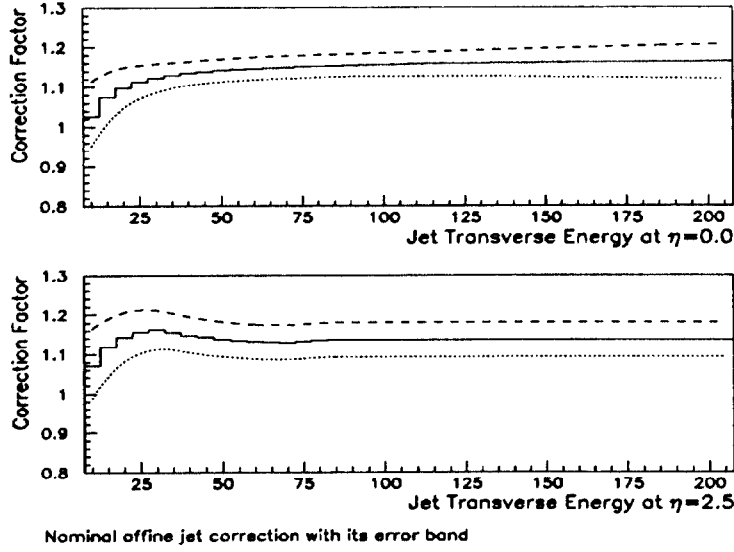


Figure 2: Correction factor for measured E_T of jet for two different η regions

$(\sigma_{E_i}/E_i) = \sigma_A\sqrt{2}$. The parametrization resulting from fits to the data [8] are shown in Figure 3 for the different parts of the detector. One clearly distinguishes the well instrumented regions in the central and forward parts of the calorimeters and the intermediate region where sampling is much more coarse. For a more detailed description of the current jet energy scale correction, see [8].

3. Transverse energy profile of jets

The fine transverse segmentation of the DØ calorimeters allows a unique measurement of the transverse energy flow profile in a jet as a function of the cone size used. At Tevatron energies this measurement has been done before by CDF [10] but in that case tracking information was used, whereas the measurement described here will use calorimeter information and thus includes neutral particles as well. The measured profile will be compared to parton shower predictions by Herwig and Isajet, but also to next to leading order (NLO) perturbative calculation at the parton level. One of the predictions of NLO QCD is the cone size dependence of any jet cross sections, which is determined by how two final state partons are distributed in a chosen cone (see sect. 4). An alternative way of studying this is to compare the calorimeter jet profile with the NLO perturbative jet profile, where the final state of a jet can either be one parton or two partons, but not more. The variable used to characterize the jet profile is the fractional energy $f(r, E_T^0)$ contained within a cone of size r as defined in Eq. 6.

$$E_T^r = \sum_i E_T^i(r') \quad i = \text{all cells with } r' < r \quad (5)$$

$$f(r, E_T^0) = E_T^r / E_T^{R^0} \quad \text{with } r < R^0 \text{ and} \quad E_T^0 = E_T^{R^0} \quad (6)$$

For this analysis, jets are found and their position and transverse energy determined with a

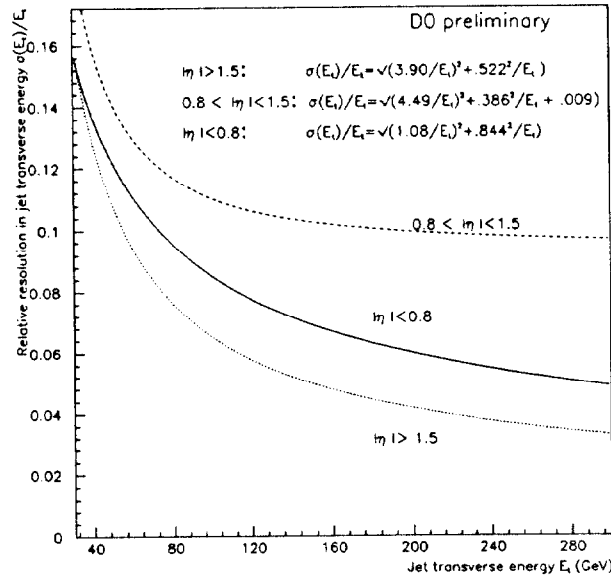


Figure 3: Relative jet E_T resolution for different rapidity regions.

cone size $R = R^0 = 1.0$. Only those jets which are not merged or split are retained for further analysis. Subsequently, with the jet direction fixed, the transverse energy is determined for cone sizes $r = 0.9$ to 0.1 . During this process a calorimeter cell is considered as part of the cone if the distance in η, ϕ between the cell center and the jet axis is $\leq r$. The transverse energies used to calculate $f(r, E_T^0)$ are *not* corrected with the jet energy scale correction, because the jet energy scale correction has only been determined for $\Delta R = 0.7$ and not for any other cone sizes yet. It is also felt that not correcting the energies introduces less systematic errors than trying to correct them. Using the Isajet Monte Carlo and varying the non-linearities in the single particle response a conservative systematic error is assigned to $f(r, E_T^0)$, which is 10% at $r = 0.1$, 2% at $r = 0.4$ and less than 1% at $r = 0.7$. The additional energy due to zero suppression (an average energy of 1.36 GeV/unit area) and the underlying event (estimated with min. bias events to be an average transverse energy of 0.55 GeV/unit area) have been subtracted. Figure 4 shows the resulting distribution for jets limited to $|\eta| < 0.2$ and with corrected transverse energy between 70 and 105 GeV. The data is plotted as a function of a variable called *subcone number*, which equals $10r + 0.5$. The errors on the data points are only statistical and in general are smaller than the symbols used. Also shown is the profile predicted by the Herwig parton shower generator and two NLO QCD predictions for two different scale choices [11]. Although not shown, the DØ results are in excellent agreement with the CDF results [10]. The experimental results seem to fall between the parton shower prediction and the perturbative NLO predictions. These results were also compared to Isajet. The Isajet results are not shown but they fall right between the DØ data points and the Herwig predictions.

In the central region the jet profile was also determined for different transverse energies of the jets. The results are displayed in Figure 5 for 4 bins in transverse energies between 45 and 140 GeV. These results again agree qualitatively with the CDF results in Ref. [10]: as the transverse energy of the jet increases, the jets become more and more collimated i.e.

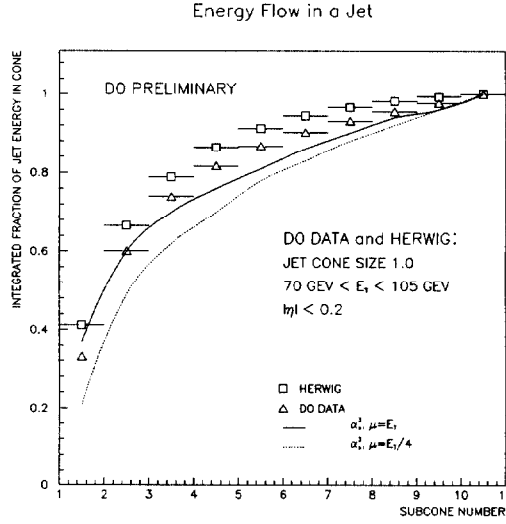


Figure 4: E_T profile for central jets compared to several predictions(see text).

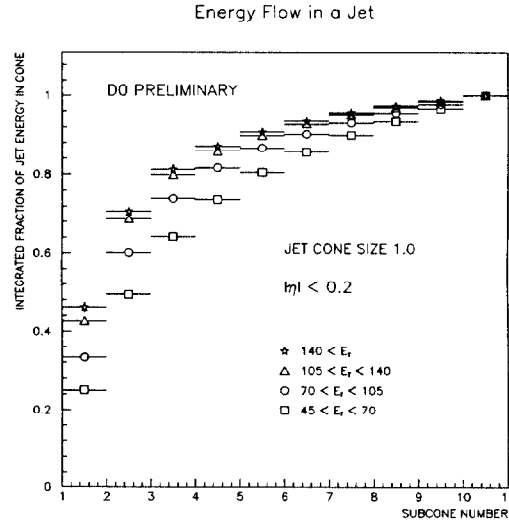


Figure 5: E_T profile for jets in central region for different E_T regions.

narrower. Similar studies are underway for jets in the forward region ($|\eta| > 2.5$) but here systematic effects due to out of cone showering are still under study.

4. Dijet final states

The production of jets in hadron collisions in the parton model is thought of as a hard scattering between two initial partons resulting in two final state partons. This, in principle, is identical to jet production at an e^+e^- collider, except that the initial state center of mass energies vary widely in a hadron collider and in addition to the electromagnetic initial state radiation there is gluon radiation resulting in additional jets. Radiation in the final state is identical in both cases. Within the framework of QCD the spectrum of initial state partons is described by the parton distributions and the hard scattering cross sections for all parton-parton combinations (i.e. $gg, gq, qq, \bar{q}q$ etc.) are determined by the appropriate hard scattering matrix elements. These matrix elements, each corresponding to a Feynman diagram to a certain order in the strong coupling constant (α_s) have been calculated up to several orders of α_s [12]. The calculation of a cross section at the parton level involves a convolution of the parton distributions with the hard scattering parton-parton cross sections. The correct calculation of such a cross section would involve the parton distributions, the hard scattering matrix elements, loop corrections to the graphs and all of this to all orders in α_s . This is technically not possible yet and, within perturbative QCD, these parton level cross sections are available now up to $O(\alpha_s^3)$ [13]. Because the calculation is not done to all orders in α_s , the results are dependent on the choice of renormalization (at which α_s is evaluated) and factorization (at which parton distributions are evaluated) scales. Typically these two scales are set equal and they are related to the hardness of the interaction i.e. the transverse momentum of the final state partons. The advantage of the $O(\alpha_s^3)$ or NLO predictions, over $O(\alpha_s^2)$ or LO predictions is that the calculated cross sections, especially the absolute scale, are less sensitive to the choice of scale[13, 14]. Unless otherwise quoted all theory predictions in this paper are evaluated at the scale: $E_T/2$. The parton distributions

used in the theory predictions are derived from lower energy experiments (for example see [15, 16]) using the perturbative QCD framework either in LO or NLO. The theory predictions used in this paper either use LO or NLO throughout, but never mix the two.

The above outlined theory predictions are all at the perturbative parton level. This implies that in the LO predictions there can at most be two and in the NLO case there can at most be three partons in the final state. In the latter case two partons can be very close and therefore can not be resolved, which leads to the necessity of defining a jet already at the parton level. The algorithm used is the fixed cone algorithm [13], which inspired the jet algorithm used in the experiment and outlined in section 2.3. This is another advantage of NLO QCD predictions: jets at the perturbative parton level and at the particle level are defined the same way. As shown in section 3. the energy profile within a jet is surprisingly well described by simply allowing one more parton to be within the jet at the parton level. Also the agreement between the total inclusive jet cross section as measured by CDF [19, 18] and DØ [3] and compared to NLO predictions is very good. For the dijet cross sections described in this chapter, an event is required to have at least two jets and its final state is characterized by the two highest E_T jets. The inclusive jet triggers, described earlier, are used as the basic samples and all corrections and cuts outlined in sections 2.3 and 2.4 are applied.

4.1 Dijet angular distributions

The angular distribution of the two jets in the center of mass system (cms) of the two initial partons is dominated by t -channel vector gluon exchange. This results in the characteristic Rutherford type angular distribution for spin=1 exchange: $dN/d\cos\theta^* = (1 - \cos\theta^*)^{-2}$, where θ^* is the angle between the incoming and outgoing partons. The shape of this distribution with its pole at $\cos\theta^* = 1$ is not very well suited for a detailed comparison between theory and experiment. For that reason the variable χ , defined in Eq. 8 is used. This variable transforms a $(1 - \cos\theta^*)^{-2}$ type distribution into a flat distribution. The relationships between the variables used to describe the dijet system are given by following equations.

$$\eta^* = \frac{\eta_1 - \eta_2}{2} \quad \cos\theta^* = \tanh\eta^* \quad \eta_{boost} = \frac{\eta_1 + \eta_2}{2} \quad (7)$$

$$M_{jj} = 2E_T \cosh\eta^* \quad \chi = e^{2|\eta^*|} = \frac{(1 + \cos\eta^*)}{(1 - \cos\eta^*)} \quad (8)$$

Here all the quantities with a $*$ are in the cms system. The inclusive cross section describing the final state is $d^3\sigma/dM_{jj}d\eta^*d\eta_{boost}$. This cross section is dependent on *i*) the parton distributions and *ii*) the hard scattering matrix elements. Integrating over large fractions of the M_{jj} and η_{boost} space results in a cross section which is relatively insensitive to the parton distributions. This normalized distribution $N^{-1}dN/d\chi$ is typically referred to as the dijet angular distribution and is shown in Fig.6 for $175 < M_{jj} < 350$ GeV and $\eta_{boost} < 2.0$. The experimental data have been corrected for trigger efficiencies and acceptance and resolution smearing. These corrections are typically less than 10% for $\chi < 25$ and can be up to 30% at $\chi \approx 200$. The error assigned to these corrections and the energy scale correction is reflected in the systematic error on the data points. The corrections were determined using the Papageno generator and using measured efficiencies and resolutions. The experimental results are compared to 3 theoretical predictions. The first one is a scaling prediction based on using

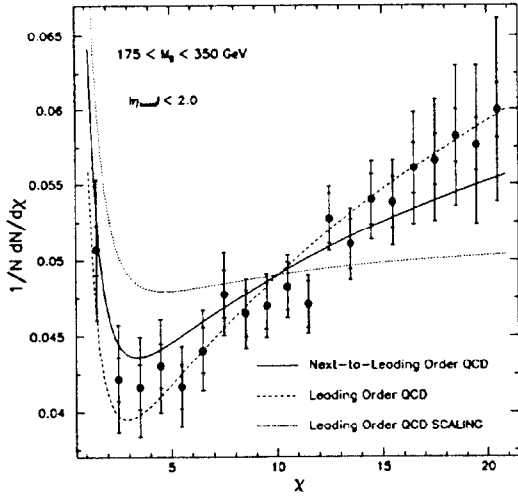


Figure 6: Dijet angular distribution for $175 < M_{jj} < 350$ GeV

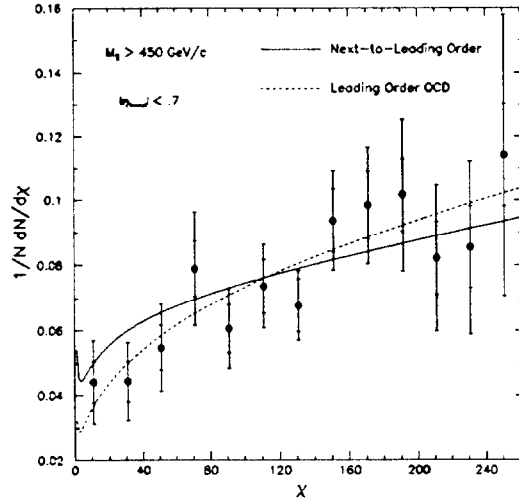


Figure 7: Dijet angular distribution for $M_{jj} > 450$ GeV

a LO QCD based calculation where parton distributions are evaluated at a fixed scale and α_s does not run but has a fixed value. This essentially corresponds to Rutherford scattering and this prediction obviously does not agree with the data. The rise at small χ is due to s -channel exchange. Including QCD corrections at LO already improves the agreement significantly (parton distributions used are Owens, set 2 [25]). Because this shape measurement is insensitive to the parton distributions, it actually represents a direct evidence for the running α_s . Including the NLO corrections makes the agreement even better [17]. Figure 7 shows the same distribution as Figure 6 but for $M_{jj} > 450$ GeV and $\eta_{\text{boost}} < 0.7$. Using a lower E_T threshold for the jets and requiring a larger M_{jj} forces η^* and thereby χ to larger values. The range in χ covered in this graph represents a tenfold increase over previous available measurements [9]. Although the error bars are larger the data still agree very well with the QCD predictions both at leading and at next to leading order. It should be emphasized that this increase in the range of χ explored is simply due to the large rapidity coverage of the D0 calorimeters.

4.1 Triple differential cross section.

As has been shown in the previous section, LO and NLO QCD predictions describe the shape of the angular distribution of the dijet system very well. This shape is determined mainly by the hard scattering matrix elements and the agreement implies that these matrix elements are necessary and correct. Given this one can ask: can the dijet cross section be used to get information about the parton distributions? This information is mainly contained in the η_{boost} and M_{jj} dependence of the cross section. To extract this information in terms of more directly measurable quantities the cross section is rewritten in the form $d^3\sigma/dE_T d\eta_1 d\eta_2$. Here now E_T can be several things: the average transverse energy of the dijet system or the transverse energy of the largest E_T jet and for this paper the latter definition is used. The other reason for writing the cross section this way is that the variables E_T, η_1 and η_2 are

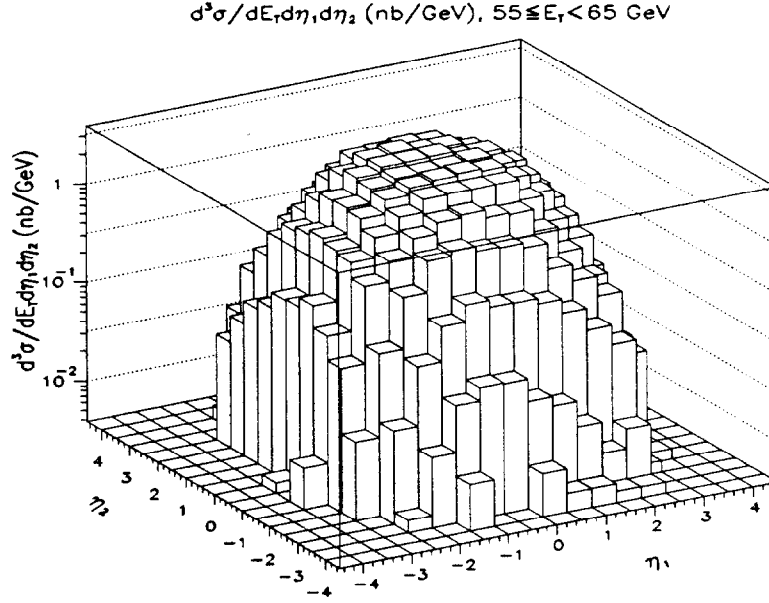


Figure 8: Measured $d^3\sigma/dE_T d\eta_1 d\eta_2$ for given E_T bin.

directly related to the x_i , the fraction of the proton momentum carried by parton i . Equation 9 gives the relationship between these variables for a simple dijet only final state.

$$x_1 = \frac{E_T}{\sqrt{s}}(e^{y_1} + e^{y_2}) \quad x_2 = \frac{E_T}{\sqrt{s}}(e^{-y_1} + e^{-y_2}) \quad (9)$$

Here E_T is the transverse energy of the jet and $\sqrt{s} = 1800$ GeV. So measuring $d^3\sigma/dE_T d\eta_1 d\eta_2$ corresponds to measuring $d^2\sigma/dx_1 dx_2$. Using NLO hard parton scattering cross sections the parton distributions can be extracted. This is similar to measuring structure functions in deep inelastic lepton scattering. Although the cross section $d^2\sigma/dx_1 dx_2$ could be extracted, it is preferred to measure the cross section in variables that are directly measurable in the detectors, so the cross section presented will be $d^3\sigma/dE_T d\eta_1 d\eta_2$. It should be emphasized that this analysis is very preliminary but it is felt that it is very promising in terms of measuring parton distributions at a hadron collider. Fig. 8 shows the measured cross section for a region $55 < E_T < 65$ GeV. Clearly the central rapidity plateau is observed and the rapid fall off with increasing rapidity.

At this point the NLO predictions for this quantity are not available yet, but it is understood that they will be soon. [20]. Visualizing a triple differential distribution is not easy, so in Figs. 9a and 9b, the same cross section is shown as function of $|\eta_2| \text{ sign}(\eta_1 \cdot \eta_2)$ for limited regions of E_T and η_1 . In one case η_1 is limited to the central region and in the other to the forward region. The x_i on the graphs indicate the regions in x probed along the distribution and the arrow configurations show what the final state jet configurations are in rapidity space. It is clear that DØ with its large rapidity coverage can probe the parton distributions down to $x = 0.002$. At these x values the cross sections are dominated by gluons so this is a unique way to directly probe the gluon distribution at the Tevatron. The data, shown with statistical errors only, are compared with two LO predictions. For both

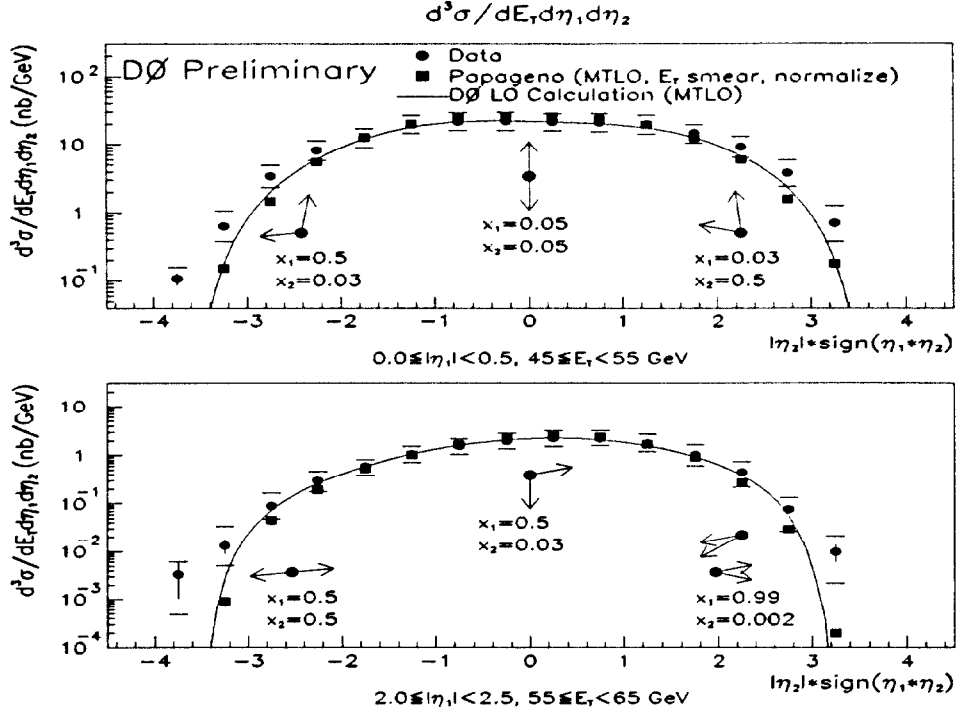


Figure 9: Projections of $d^3\sigma/dE_T d\eta_1 d\eta_2$ for a given E_T range and two η_1 regions, compared to LO QCD predictions.

cases the Morfin-Tung LO parton distributions [21] are used and the absolute normalization is the same as the data. In one the generator Papageno is used and the predictions are smeared with jet energy resolution. The other prediction is based on an analytical parton level LO dijet cross section calculation done internally within the experiment [22]. In general it can be concluded that the shapes agree rather well with the LO predictions, except for the far forward regions. More work on the experimental side is needed in understanding the acceptances in the forward regions and on the theoretical side NLO predictions are needed.

5. A test of resummation

Recently a calculation which resums higher order corrections to jet final states by Del Duca and Schmidt [23] has been completed. It gives corrections to jet cross sections coming from multiple radiations in the initial and final state. These radiations turn the simple two jet final state into a multi jet final state, resulting in many low energy jets (often referred to as mini-jets) in the final state at the parton level. In a simple minded picture this works as follows: at leading order the final state consist of exactly two partons. As higher and higher orders are allowed to contribute (in the calculation) the clear two jet picture disappears and is replaced by a final state of multiple jets which spread over all rapidity. The above mentioned calculation uses resummation techniques to predict how this evolution should take place and a particular test has been suggested: Select events with at least one jet with $E_T > 50$ GeV, which corresponds to one of the DØ triggers. For all jets in the event with $E_T > 12$ GeV find the pair (E_T^1, η_1) and (E_T^2, η_2) for which $\Delta\eta = |\eta_1 - \eta_2|$ is the largest. Require $50 < E_T^1 < 55$ GeV and determine $d^3\sigma/dE_T^1 dE_T^2 d(\Delta\eta)$. The only additional cut applied is that $\eta_{boost} < 0.5$, where η_{boost} is defined in Eq. 7. Fig. 10 shows the theoretical prediction for

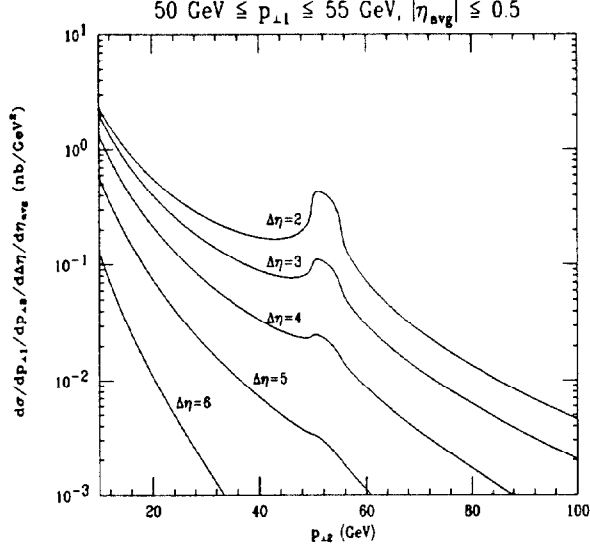


Figure 10: Theory prediction for the correlation.

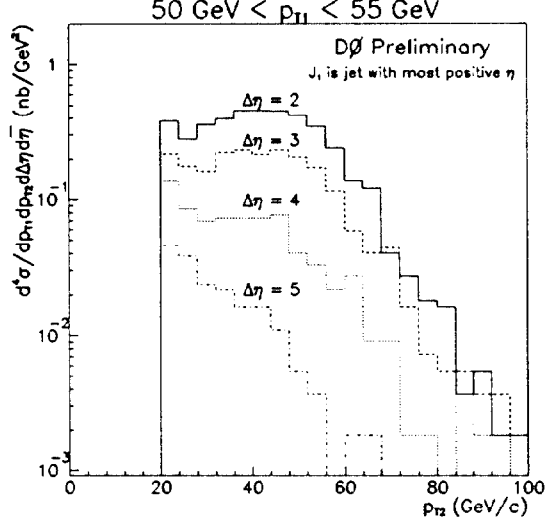


Figure 11: DØ measurement of the correlation.

this quantity [26]. It illustrates that with increasing rapidity separation between the jets, the correlation in E_T vanishes. Figure 11 displays the preliminary experimental result, which is qualitatively in very good agreement with the prediction. The ultimate goal of this analysis is to do an absolute comparison between experiment and theory.

It has been suggested that the predicted decorrelation is simply a kinematic effect and that could very well be true. To that end simulations with more standard parton shower Monte Carlos are underway. However the work by Del Duca and Schmidt has shown experimentalists a new way to look at data which cover a large range in rapidity and that in itself is already a very useful contribution.

6. Topology of 3 jet events

The structure of three jet events in terms of relative momentum distributions and spatial distributions can be used to compare theory and data. The theoretical predictions are obtained by using two different approaches: *i*) an $O(\alpha_s^3)$ tree level prediction (Papageno at the parton level) and *ii*) leading order parton shower type Monte Carlos: Herwig and Pythia. Three jet events are taken from the trigger sample where at least one jet with $E_T > 50$ GeV was required. All the standard jet cuts and corrections were applied and the final selection criteria are:

- at least three jets with $E_T > 20$ GeV
- at least one jet with $E_T > 60$ GeV
- mass of jet system $M_{jjj} > 250$ GeV
- separation between any jet pair in η, ϕ space > 1.4

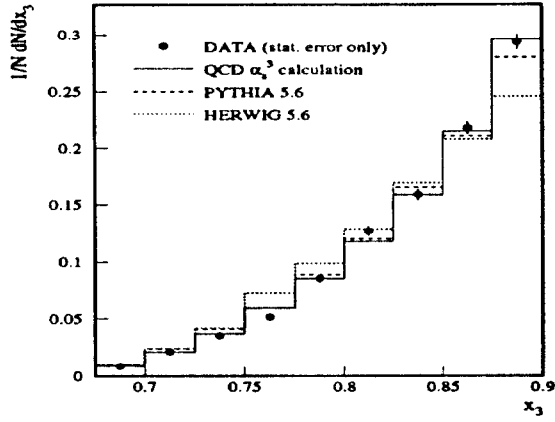


Figure 12: The scaled energy distribution of the leading jet.

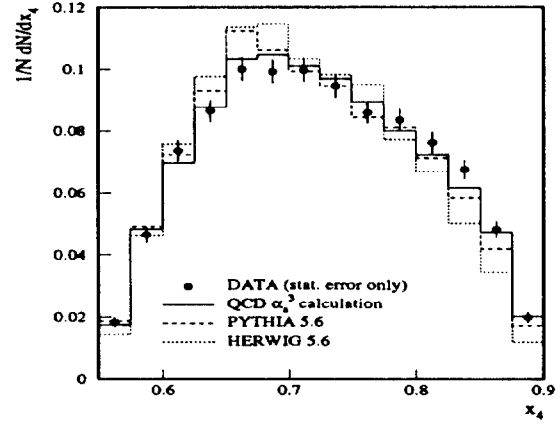


Figure 13: The scaled energy distribution of the next to leading jet.

Using these criteria the final event sample consists of 7200 events. Assuming massless partons, the topology of a three parton final state in its cms system can be described in terms of 6 variables. Three of the variables define how the cms energy is shared among the three final state partons. The other three define the orientation of the planes containing the three partons in space. It is convenient to introduce the notation: $1 + 2 \rightarrow 3 + 4 + 5$ for the three parton final state process. Number 1 and 2 refer to the incoming partons, while 3, 4 and 5 label the outgoing partons, ordered in descending cms energies i.e. $E_3 > E_4 > E_5$. The final state parton energies are typically expressed by scaled variables $x_i = 2E_i/\sqrt{\hat{s}}$, where \hat{s} is the three jet cms energy. This implies that: $x_3 + x_4 + x_5 = 2$, so only two of the scaled variables are necessary to describe the process. The angular variables are chosen to be: *i*) the polar angle (θ_3^*) of parton 3 with respect to the beam, *ii*) the azimuthal angle (ϕ_3^*) of parton 3 and *iii*) the angle (ψ^*) between the plane containing parton pair (1,3) and the plane containing parton pair (4,5). For unpolarized beams the ϕ_3^* distribution is uniform. Therefore only four independent kinematic variables are needed to describe the topology of the three jet system and they are chosen to be: $x_3, x_4, \cos\theta_3^*$ and ψ^* .

Figure 12 and 13 show the the distributions for x_3 and x_4 and the different theoretical predictions. For this comparison the DO, set 1 parton densities [25] was used and the measured distributions are directly compared to parton level predictions, because it was found that the corrections for acceptances and resolution were typically of order 5%. The tree level $O(\alpha_s^3)$ calculation agrees very well with the data for both variables x_3 and x_4 . The main features of the distributions are reproduced by Pythia and Herwig, but they show a deficit in both distributions near $x = 1$.

The $\cos\theta_3^*$ distribution is shown in Figure 14. Similar to the angular distribution for dijet events, the characteristic Rutherford scattering is clearly visible. The large rapidity coverage of the calorimeters allows this analysis to $\cos\theta_3^* = 0.95$. As evident in the figure, the data are well reproduced by the $O(\alpha_s^3)$ prediction. Also evident is a surplus by Pythia and a deficit by Herwig in the relative rate estimation at small values of $\cos\theta_3^*$.

The ψ^* distribution is a probe of initial state radiation and it is shown in Figure 15. The

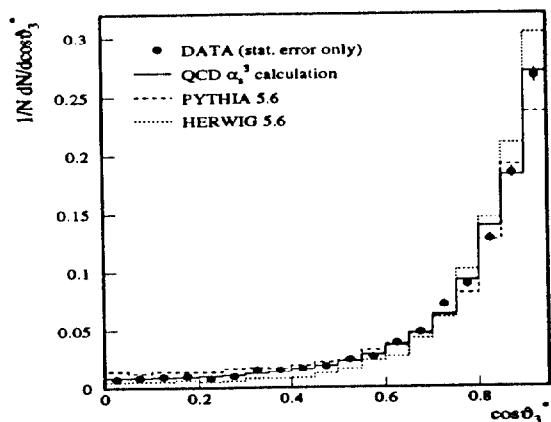


Figure 14: Distribution of $\cos \theta_3^*$ of the leading jet.

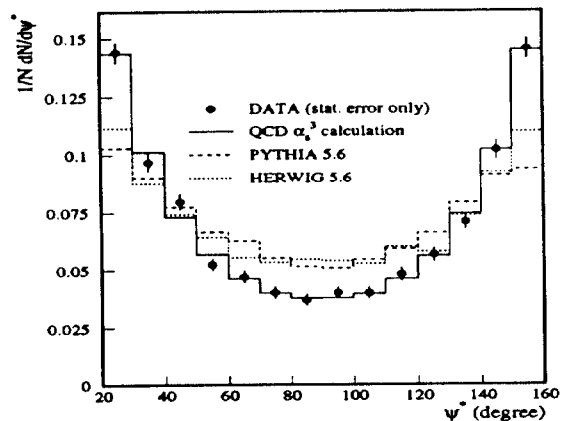


Figure 15: Distribution of ψ^* , the angle between the planes defined in the text.

enhancement due to initial state radiation at $\psi^* = 20^\circ$ and $\psi^* = 160^\circ$ is clearly visible. As in the previous comparisons, the agreement between data and the $O(\alpha_s^3)$ prediction is excellent. However both Herwig and Pythia fail to correctly describe the measured distribution. This disagreement implies that the relative contribution of the initial state radiation is not well accounted for by these parton shower Monte Carlos.

7. Summary

Since August of 1992 when the DØ detector began taking data there has been enormous progress in the understanding of jet final states in terms of trigger, algorithm and reconstruction and many analyses have been started with the data accumulated. The principle avenue for obtaining the correct jet energy scale in the whole detector has been established and outlined here. The understanding of the jet energy scale and jet energy resolution has vastly improved since data taking started. The excellent calorimetry will make it possible to significantly reduce the currently large systematic errors. This is still an area of very active study. The fine segmentation of the calorimeter allows detailed studies of the internal jet shape and first results indicate good agreement with previous CDF results obtained from tracking information. A major new contribution in jet physics by DØ is the extension of the current available rapidity range into unexplored regions up to $\eta = 3$ and beyond. This is clearly demonstrated in the dijet angular distributions where the explored range in the variable χ has increased tenfold compared to previous results. The rapidity coverage also allows the measurement of the true triple differential dijet cross section and new tests of resummation techniques. Very preliminary results for both analyses show potential to explore new areas within QCD jet physics. A more traditional analysis of the topology of the three jet final state has been presented and shows that widely separated jets are better described by tree level predictions at the parton level than by parton shower generators. From the preliminary results of several analyses presented, it is clear that the DØ experiment is in a position to do new and unique QCD studies with jet final states.

References

- [1] DØ collaboration, S. Abachi *et al.*, Nucl. Instr. & Meth. **A338**, 185 (1994) or Fermilab-Pub-93/179-E.
- [2] N. Graf, "Production of W and Z bosons at DØ", these proceedings.
- [3] J. Kotcher, "Inclusive Jet and Photon Production at the DØ Experiment", these proceedings.
- [4] F. Borchering, "Rapidity Gaps and Color Coherence in Jet Final States", these proceedings.
- [5] S. Abachi *et al.*, Nucl. Instr. & Meth., **A324**, 53 (1993)
- [6] N. Hadley, DØ internal note 904 (1989)
- [7] Proc. of the 1990 Summer Study on HEP, July 1990, Snowmass, Colorado, World Scientific, p.134-136, J. Huth *et al.* (Snowmass Jet Accord).
- [8] A. Milder, Ph.D. thesis, University of Arizona, 1993
- [9] CDF collaboration, F. Abe *et al.*, Phys. Rev. Lett. **69**, 2896 (1992)
- [10] CDF collaboration, F. Abe *et al.*, Phys. Rev. Lett. **70**, 713 (1993)
- [11] These predictions were taken from figure 1 in Ref. [10].
- [12] Z. Kunzst and E. Pietarinen, Nucl. Phys. **B164**, 45 (1980); T. Gottschal and D. Sivers, Phys. Rev. **D21**, 102 (1980); R.K. Ellis and J.C. Sexton, Nucl. Phys. **B269**, 445 (1986); F.A. Berends *et al.*, Nucl. Phys. **B333**, 120 (1990) and references therein
- [13] S. Ellis, Z. Kunzst, D. Soper, Phys. Rev. Lett. **62**, 726 (1989) and Phys. Rev. **D40**, 2188 (1989); Phys. Rev. Lett. **64**, 2121 (1990)
- [14] S. Ellis, Z. Kunzst, D. Soper, Phys. Rev. Lett. **69**, 1496 (1992)
- [15] J.F. Owens and W.K. Tung, Parton Distributions of Hadrons, in Ann. Rev. Nucl. Sci. (1992)
- [16] J. Botts *et al.*, Phys. Lett. **B304**, 159 (1993)
- [17] for NLO the scale: $0.5M_{jj}/2\cosh(0.7\eta^*)$ is used as suggested in [14]
- [18] S. Kuhlmann, "CDF QCD Overview", these proceedings.
- [19] CDF collaboration, F. Abe *et al.*, Phys. Rev. Lett. **68**, 1104 (1992)
- [20] S. Ellis and D. Soper, private communication.
- [21] J.G. Morfin, W.K. Tung, Z. Phys. **C52**, 13 (1991)

- [22] S. Feher and P. Mooney, DØ internal note 1919 (1993).
- [23] V. Del Duca and C. Schmidt, preprint DESY 93-139/SCIPP 93/35
- [24] Jianming Qian, DØ internal note 1868 (1993).
- [25] D.W. Duke and J.F. Owens, Phys. Rev. **D30**, 49 (1984);
J.F. Owens, Phys. Lett. **B266**, 126 (1991)
- [26] This figure was kindly supplied by V. Del Duca, see ref. [23].